

Electromagnetic Models for Passive Detection and Localization of Multiple Bodies

Vittorio Rampa, Gian Guido Gentili, Stefano Savazzi, and Michele D'Amico

Abstract—The paper proposes a multi-body electromagnetic (EM) model for the quantitative evaluation of the influence of multiple human bodies in the surroundings of a radio link. Modeling of human-induced fading is the key element for the development of real-time Device-Free (or passive) Localization (DFL) and body occupancy tracking systems based on the processing of the Received Signal Strength (RSS) data recorded by radio-frequency devices. The proposed physical-statistical model, is able to relate the RSS measurements to the position, size, orientation, and random movements of people located in the link area. This novel EM model is thus instrumental for crowd sensing, occupancy estimation and people counting applications for indoor and outdoor scenarios. The paper presents the complete framework for the generic N-body scenario where the proposed EM model is based on the knife-edge approach that is generalized here for multiple targets. The EM-equivalent size of each target is then optimized to reproduce the body-induced alterations of the free space radio propagation. The predicted results are then compared against the full EM simulations obtained with a commercially available simulator. Finally, experiments are carried out to confirm the validity the proposed model using IEEE 802.15.4-compliant industrial radio devices.

Index Terms—Electromagnetic diffraction, EM Body Model, Radio propagation, Wireless Sensor Networks.

I. INTRODUCTION

HUMAN Presence-aware Systems (HPSs) are rapidly growing as new services become available in various areas of modern life [1] such as assisted living, ambient intelligence, smart spaces, home automation, human-robot collaboration, safety and security, just to cite a few. Among these applications, non-cooperative, also known as passive, HPS are the most attractive since they do not require the monitored users to carry or wear any electronic device or specific sensors. Usually, these systems are vision-based [2]–[4]; however, the ubiquitous presence of wireless networks paves the way towards the exploitation of wireless radio-frequency (RF) networks, not only as communication devices, but also as body proximity/location virtual sensors. Last but not least, radio-based HPS are privacy-neutral since they do not reveal any privacy information about the monitored people.

HPS systems exploit the fact that people, or obstacles, in the surroundings of an area covered by a wireless radio network induce signal alterations that can be detected and exploited for

body occupancy inference applications. For instance, Device-Free Localization (DFL) systems [5], [6] exploit a network of RF nodes to detect the presence, to locate and track the position of moving objects or people in a confined area covered by the wireless network itself. However, a radio-based HPS is not only able to localize and track [7]–[9] people, or objects, but it has been also proven to efficiently perform other tasks such as to count the number of people [10], to identify and recognize patterns related to their activities [11], [12] and intentions [11], to detect dangerous worker conditions and safety status [13], [14], and act as a proximity monitor [15]. This is made possible as the presence of targets (*i.e.*, objects or people) affects the propagation of the radio waves in the covered area [16], [17], for example by inducing predictable alterations of the Received Signal Strength (RSS) field that depend on the targets position, in both static [18] and dynamic [19] environments.

A. Related works

The effect of the presence of people on the received RF signals is a well know topic [20], [21] and finds its roots in the research activities about the electromagnetic (EM) propagation phenomena caused by natural or artificial obstacles during the first experimental trials at the dawn of the radio era [22]. These studies have received a great impulse after the middle of the last century mostly for outdoor coverage applications [23]–[26]. However, despite some recent attempts to model the body-induced fading effects on short-range radio propagation [27], these research activities are mostly related to inter- [28], [29] and intra-body [30], [31] short-range radio communications. The aim of these research activities is to quantify the radio propagation losses in narrow [32] or wide-band [33] indoor scenarios with the main purpose of mitigating these effects. Only a few research works [28], [34], [35] focus their attention on the geometrical relations between the transmitter (TX) and receiver (RX) location, the position and composition of the body, and its size.

A general EM model for the prediction of the mathematical relations between location, size and composition of a *single-target* and the corresponding EM field perturbation, is still disputable as shown in [36], [37] or too complex to be of practical use as based on ray tracing techniques [29], [38] or Uniform Theory of Diffraction (UTD) [28], [35]. Other EM methods [39]–[41] and physical-statistical models [38], [42]–[44] are simpler than the previous ones but still limited to a single target. To the authors knowledge, and according to the current literature, an analytical, or semi-analytical, approach

V. Rampa and S. Savazzi are with the Istituto di Elettronica, di Ingegneria dell'Informazione e delle Telecomunicazioni (IEIIT), Consiglio Nazionale delle Ricerche (CNR), Milano, Italy, e-mail: vittorio.rampa, stefano.savazzi@ieiit.cnr.it. G. G. Gentili and M. D'Amico are with the Dipartimento di Elettronica, Informazione e Bioingegneria (DEIB), Politecnico di Milano, Milano, Italy, e-mail: gianguido.gentili, michele.damico@polimi.it. This preprint has been submitted to IEEE for possible publication.

towards a *true multi-body* model has never been tackled before. Usually, multi-target (*i.e.*, multi-body) problems have been solved by assuming the linear superposition of the single-body extra attenuations [7], [17]. However, the mutual effects induced by multiple bodies moving concurrently in the same space must be accounted for.

In [8] a DFL system has been proposed to track two targets moving concurrently by using an EM model that is fully described in [45]. On the contrary, in this paper, the model is generalized to an *arbitrary number of targets*. A practically-usable physical-statistical model is thus designed for the prediction and the evaluation of the body-induced propagation losses, namely the RSS field, found in true N -targets scenarios with $N \geq 1$. This N -body model is able to describe both dominant static component and stochastic fluctuations of the power loss as a function of the locations of the N targets, their size, orientation and random movements with respect to the link path.

B. Original contributions

The paper proposes an EM framework where the field perturbations induced by an arbitrary number of human bodies are modelled as a superposition of *diffraction* and *multipath* terms. The diffraction component is defined according to the scalar diffraction theory and is characterized by the geometrical description (*i.e.*, location, size, orientation) and the movement characteristics (*i.e.*, rotations and random movements around the nominal position) of N targets according to the knife-edge hypothesis [24], [46]–[48]. The multipath fading term is assumed to impair the radio link due to the presence of the bodies placed inside the sensitivity area [49] around the LOS (Line Of Sight) path that connects the transmitter and the receiver. However, unlike [49], where RSS perturbations are predicted for a *single small* target [25], [49], [50] moving only in the central part of the LOS path according to the paraxial approximation [49], this novel model provides a representation of the power losses induced by *multiple* bodies having *any* size, and placed *anywhere* in the area surrounding the radio link. The model presented here extends the dual-body case exploited in [8] and then presented in [45], by considering a generic EM scenario with an arbitrary number of human bodies in the surroundings of a radio link. In the former reference [8], the dual-body model is neither derived nor justified but it is just introduced to perform DFL tasks and compare the results against other methods. In the latter reference [45], the dual-body model is derived from prime principles and then described and discussed in details. The experimental results presented here confirm that the proposed model can effectively describe the mathematical relations between the target positions and the measured RSS values. Comparisons with the results obtained with the EM simulator Feko also support the validity of the proposed model.

The novel contributions of this paper are: *i)* the definition of a general EM framework for the multi-body scenario; *ii)* the derivation, from prime principles, of the full equations for the prediction of the global extra attenuation due to N bodies, or objects, in the LOS area; *iii)* the derivation of the analytical

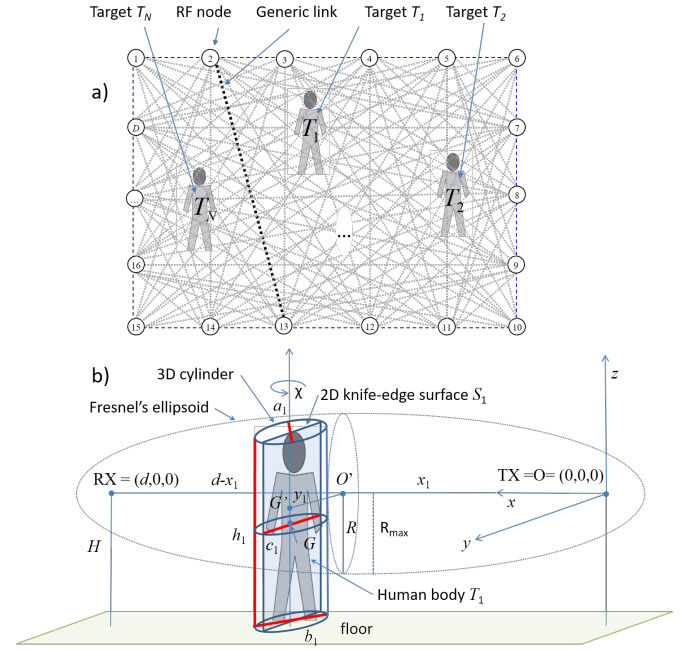


Figure 1. a) Generic layout of a HPS-based wireless network composed by D nodes and L links where T_n is the n -th target located inside the monitored area; b) Simplified representation of the single-link single-body scenario where the human body T_1 is sketched as a 3D cylinder and then simplified as a 2D knife-edge surface S_1 .

formulas in the case of paraxial hypothesis for the general N bodies scenario; *iv)* the evaluation of the extra attenuation predictions for the dual-body scenario (*i.e.*, $N = 2$) and their comparison against the results obtained using full EM simulations; and *v)* tuning of the dual-body model parameters based on-field RSS measurement trials and comparisons of the model predictions against the aforementioned RSS measurements.

The paper is organized as follows. The diffraction model that accounts for the deterministic term of the multi-body induced extra attenuation is shown in Sect. II for any number N of the targets. The complete physical-statistical model for the prediction of the RSS field is illustrated in Sect. III. In particular, the dual-body model is highlighted as a practical case study. Sect. IV deals with the evaluation of the proposed multi-target model featuring a comparative analysis against experimental measurements and simulation results. The concluding remarks are drawn in Sect. V.

II. DIFFRACTION FRAMEWORK FOR THE MULTI-BODY SCENARIO

As sketched in Fig. 1.a, a generic HPS consists of a mesh of partially, or completely connected, wireless network composed of D RF nodes [5], [6] and $L \leq D(D-1)/2$ bidirectional links. The HPS-enabled network is composed by nodes that are able to perform power measurements on the RF signal and, after some processing steps, to extract body occupancy-related information. We assume that all the RF nodes can measure the RSS field values at discrete time instants. No specific additional RF hardware [6] is required since RSS values are computed in the normal operations of the networked RF nodes for channel estimation/equalization and frequency/frame synchronization tasks.

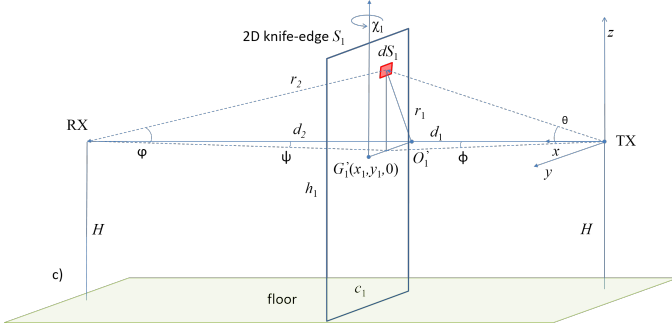


Figure 2. Geometrical representation of the same scenario shown in 1.b, where an horizontal link of length d is positioned at distance H from the floor and a 2D knife-edge surface S_1 , with variable traversal size c_1 and height h_1 , represents the body T_1 that is placed on the floor.

Without any loss of generality, as described in Fig. 1.b, in what follows, we will focus on the single-link scenario (*i.e.*, $L = 1$ and $D = 2$), by introducing the single-target (T_1 being $N = 1$) first and then the multi-target (T_1, \dots, T_N with $N > 1$) cases. However, the multi-body model presented here can be exploited in a general multi-link scenario with D nodes, L links and N targets by using electric field superposition. In addition, it can be extended to make use of other physical layer channel information measures such as the Channel State Information (CSI) and the Channel Quality Information (CQI) [6] as well. However, this discussion is outside the scope of this work.

It is worth noticing that all the proposed models apply to a generic link of the radio network: therefore, they could be easily tailored to predict RSS over arbitrarily complex network structures for more robust body positioning, as proposed in device-free localization methods [6], [7], [17]. In addition, modeling of RSS is instrumental for link selection operations, namely to identify an optimized subset of links that are most influenced by the target presence [8].

A. Single body model (SBM)

The single body model [43] is briefly recalled in this section since it is the starting point for the multi-target model that will be described in Sect. II-C. As outlined in Fig. 2, the human body (*i.e.*, the only target T_1 located near the single-link area) is represented by a perfectly EM absorbing 3D homogeneous cylinder with an elliptical base of minor and major axes a_1 and b_1 , respectively, that simulate the human head, torso, legs and arms (placed near the torso). Most references assume a 3D cylinder with a circular base [35], [51] or a prism [29] while only a few [34], [52] assume also that the arms can freely move with respect to the torso. Considering a dynamic scenario where the 3D cylinder, modeling the body, can freely move horizontally and rotate around its generic *nominal* position (x, y, z) showing different views, the target is reduced [43] to a 2D rectangular blade (*i.e.*, a knife-edge surface) [47], orthogonal to the LOS path at distance d_1 and d_2 from the TX and RX, respectively. The knife-edge surface is vertically placed close to the link area and can freely rotate and move showing different body views during its movements. The presence of the floor does not imply any influence on

the EM propagation and it is used here only for geometrical reasons *i.e.*, to define the height of the link and the placement constraints of the knife-edge surface representing the body. Notice that the knife-edge approximation ignores important EM parameters such as polarization, permittivity, conductivity, shape, radius of curvature, and surface roughness [53].

According to the Fig. 1.b, the radio link is horizontally placed at distance H from the floor and the 3D target T_1 , that is placed on the floor, is free to move and rotate around the vertical axis in the surroundings of the LOS path. The corresponding first Fresnel's zone ellipsoid [47], with radius $R = \sqrt{\lambda d_1 d_2 / d}$, does not have any contact with all other parts of the scenario (*e.g.*, walls, ceiling, furniture or other obstacles) except for the aforementioned target. Being $R \leq R_{\max} = \sqrt{\lambda d} / 2$, where R_{\max} is the maximum value of the radius R , λ is the wavelength and d is the RX-TX distance (*i.e.*, the link path length), this constraint becomes $2H > \sqrt{\lambda d}$. Notice that, as stated by standard short-range indoor propagation models [54], ground attenuation effects may be safely ignored for a radio link inside a single indoor large room/space *e.g.* a hall.

The equivalent 2D knife-edge surface S_1 has height h_1 , width c_1 , and it is placed orthogonal to the LOS path at location $\mathbf{X}_1 = [x_1, y_1]^T$. \mathbf{X}_1 coincides with the first two coordinates of the S_1 barycenter $G_1 = (x_1, y_1, z_1)$ of the knife-edge S_1 since z_1 assumes the constant value $z_1 = h_1/2 - H$. The point G'_1 is the intersection of the vertical axis passing through G_1 and the horizontal plane $z = 0$. In the followings, the position of the target T_1 (*i.e.*, the position of G'_1) is thus identified by the off-axis displacement y_1 and the distance $x_1 = d_1$ of S_1 from the TX. However, a true person can also turn and make involuntary/voluntary movements while standing on the floor. Therefore, the 3D target T_1 , represented by the 2D knife-edge surface S_1 , can assume any orientation $\chi_1 \in [-\pi, \pi]$ with respect to the LOS path. It can make also some small movements $\Delta \mathbf{X}_1 = [\Delta x_1, \Delta y_1]^T$ around the nominal location \mathbf{X}_1 thus showing a changing traversal size $c_1 = c_1(\chi_1) \in [a_1, b_1]$ and location $\mathbf{X}_1 + \Delta \mathbf{X}_1$.

According to the scalar theory of diffraction, the electric field at the RX, that is generated by the isotropic source in TX is modified by the presence of the 2D knife-edge surface S_1 located in the link area [43]. It can be predicted [25] as being generated by a virtual array of Huygens' sources located on S_1 but not belonging to the obstacle itself. In far field conditions, the electric field dE at the RX due to the diffraction effects caused by the elementary Huygens' source of area dS_1 with generic coordinates (x, y, z) is given by

$$dE = j \frac{E_0 d}{\lambda r_1 r_2} \exp \left\{ -j \frac{2\pi}{\lambda} (r_1 + r_2 - d) \right\} dS_1, \quad (1)$$

where r_1 and r_2 are the distances of the generic elementary area dS_1 for the TX and RX, respectively. E_0 is the free-space electric field that is described by the following equation

$$E_0 = -j \frac{\eta I \ell}{2 \lambda d} \exp \left(-j \frac{2\pi d}{\lambda} \right), \quad (2)$$

with η being the free-space impedance and $I \ell$ the momentum of the source. The electric field at the RX is given by [43]

$$E = -j \frac{\eta I \ell}{2 \lambda d} \exp \left(-j \frac{2 \pi d}{\lambda} \right) \cdot \left\{ 1 - j \frac{d}{\lambda} \int_{S_1} \frac{1}{r_1 r_2} \exp \left\{ -j \frac{2 \pi}{\lambda} (r_1 + r_2 - d) \right\} dS_1 \right\}, \quad (3)$$

where the first term refers to the electric field (2) due to the free-space propagation in the empty scenario and the second term includes the diffraction effects due to the body presence according to Eq. (1). The integral of the second term, is computed over the rectangular domain defined by the S_1 region defined as $S_1 = \{(x, y, z) \in \mathbb{R}^3 : x = x_1 = d_1, y_1 - c_1/2 \leq y \leq y_1 + c_1/2, -H \leq z \leq h_1 - H\}$. Focussing on the *extra attenuation* induced by the body *w.r.t.* the free-space, Eq. (3) can be written as

$$\frac{E}{E_0} = 1 - j \frac{d}{\lambda} \int_{S_1} \frac{1}{r_1 r_2} \exp \left\{ -j \frac{2 \pi}{\lambda} (r_1 + r_2 - d) \right\} dS_1. \quad (4)$$

According to (4), the presence of the body induces an extra attenuation $A_{dB} = -10 \log_{10} |E/E_0|^2$ *w.r.t.* the free-space propagation. Being a forward only method, the diffraction model holds only for the generic target T_1 placed in the area \mathcal{Y} near the radio link where it is $\mathcal{Y} = \{(x, y) \in \mathbb{R}^2 : 0 < x < d; -\infty < y < +\infty\}$. Of course, as shown in [43], the effect of the target presence vanishes for large but finite values of $|y|$.

B. Paraxial single body model (PSBM)

By exploiting the paraxial approximation and the following variable substitution $u = y \frac{\sqrt{2}}{R_1}$ and $v = z \frac{\sqrt{2}}{R_1}$, Eq. (4) reduces to the PSBM (Paraxial Single Body Model) equation defined as

$$\frac{E}{E_0} = 1 - \frac{1}{2} j \int_{(\sqrt{2}y_1 - c_1/\sqrt{2})/R_1}^{(\sqrt{2}y_1 + c_1/\sqrt{2})/R_1} \exp \left(-j \frac{\pi}{2} u^2 \right) du \cdot \int_{-\sqrt{2}H/R_1}^{+\sqrt{2}(h_1 - H)/R_1} \exp \left(-j \frac{\pi}{2} v^2 \right) dv, \quad (5)$$

where the Fresnel's radius $R_1 = R(x_1)$ is given by $R_1 = \sqrt{\lambda x_1 (d - x_1)/d}$. Here, we have specified that the generic Fresnel's radius R of Fig. 1.b is equal to $R(x_1)$ to explicitly highlight that it is related to the position x_1 of target T_1 . Eq. (5) can be easily computed by using the Fresnel's Sine and Cosine Integrals [49]. The paraxial approximation implies the following assumptions: $\max\{|y_1|, |z_1|, h_1, c_1, \lambda\} \ll \min\{x_1, d - x_1\}$, $\cos \varphi \simeq 1$, $\cos \theta \simeq 1$, $\cos \psi \simeq 1$, and $\cos \phi \simeq 1$, where the aforementioned angles are shown in Fig. 2. The model gives valid predictions in the same area \mathcal{Y} defined for the SBM model. The paraxial approximation is mainly used for outdoor scenarios, namely for terrestrial radio propagation applications [23], [24] where it holds gracefully. However, it has been also employed in HPS applications [55], even if this paraxial hypothesis limits the validity of Eq. (5) for small bodies near the central area of the radio link. For more details about single target modeling derived from (4), *e.g.* for

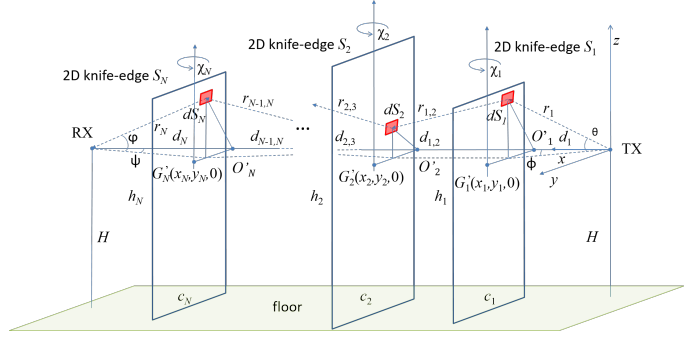


Figure 3. Single-link multi-target ($N > 1$) scenario composed by an horizontal single-link of length d , placed at distance H from the floor, and N different 2D equivalent knife-edge surfaces S_1, S_2, \dots, S_N corresponding to the targets T_1, T_2, \dots, T_N located in $\mathbf{X}_1, \mathbf{X}_2, \dots, \mathbf{X}_N$, respectively.

models that include vertical or horizontally polarization, the interested reader can refer to [43].

C. Multi-body model (MBM)

According to Fig. 3, the multi-body scenario is a generalization of the single-target case shown in Fig. 2. N knife-edge surfaces stand vertically on the floor and are placed orthogonally to the LOS path. They are numbered from 1 up to N according to their increasing distances from the TX. Knife-edge positions are identified by the column vectors $\mathbf{X}_n = [x_n, y_n]^T$ that correspond to the projections $G'_n = (x_n, y_n, 0)$ of knife-edge barycenters $G_n = (x_n, y_n, z_n)$ with $z_n = h_n/2 - H$. The positions of all targets are thus identified by the column vector $\mathbf{X} = [\mathbf{X}_1^T \mathbf{X}_2^T \dots \mathbf{X}_N^T]^T$. The single n -th target T_n , with $1 \leq n \leq N$, is described by the rotating knife-edge surface S_n having height h_n , traversal size $c_n = c_n(\chi_n)$ with constraint $a_n \leq c_n \leq b_n$ and orientation $\chi_n \in [-\pi, \pi]$ *w.r.t.* the LOS path, with obvious meaning of these terms already mentioned in Sect. II-A. All geometrical and motion parameters are organized in the following column vectors: $\mathbf{a} = [a_1, a_2, \dots, a_N]^T$, $\mathbf{b} = [b_1, b_2, \dots, b_N]^T$ collecting the knife-edges traversal sizes, $\mathbf{h} = [h_1, h_2, \dots, h_N]^T$ the target heights and $\boldsymbol{\chi} = [\chi_1, \chi_2, \dots, \chi_N]^T$ the corresponding orientations. Finally, $\forall \Delta x_n, \Delta y_n \in [-B + B]$, the column vector $\boldsymbol{\Delta X} = [\boldsymbol{\Delta X}_1^T \boldsymbol{\Delta X}_2^T \dots \boldsymbol{\Delta X}_N^T]^T$ tracks the involuntary/voluntary movements of the bodies in the position interval $[-B + B]$ (supposed symmetrically arranged) around the nominal position vector \mathbf{X} .

For $N > 1$ targets, the knife-edge diffraction model (1) still holds true for each n -th surface S_n , although equation (4) is no longer valid. The LOS path is now divided into $N + 1$ segments of length equal to $d_1, d_{1,2}, d_{2,3}, \dots, d_{N-1,N}, d_N$ with $d = d_1 + \sum_{n=1}^{N-1} d_{n,n+1} + d_N$. Generalizing the model of Sect. II-A for N targets, the term $r_{n,n+1}$ represents the distance between two consecutive elementary areas dS_n and dS_{n+1} while the terms r_1 and r_N represent the distance between the transmitter and dS_1 , and the distance between dS_N and the receiver, respectively. The n -th elementary area $dS_n = d\xi_n d\zeta_n$ is located on the n -th plane S_n that is identified by its position \mathbf{X}_n . The coordinate axes ξ_n and ζ_n (for clarity not shown in Fig. 3) have the origin in O'_n and are directed as the y and z axes. As an additional hypothesis with respect to

the ones of Sect. II-A, only forward propagation from TX to RX is considered with no backward scattered waves between any surfaces S_n and the RX (*i.e.*, both single- and multiple-scattering effects between knife-edges are ignored).

In far field conditions, by assuming only forward propagation, $\forall T_n$ with $n = 1, \dots, N-1$, the elementary electric field dE_{n+1} due to the diffraction effects caused by the elementary Huygens' source of area dS_n , is computed at dS_{n+1} by considering the distance $r_{n,n+1}$ between the elements dS_n and dS_{n+1} according to

$$dE_{n+1} = j \frac{dE_n dS_n}{\lambda r_{n,n+1}} \exp \left(-j \frac{2\pi r_{n,n+1}}{\lambda} \right). \quad (6)$$

The electric field E_1 , impinging on the first target, is

$$E_1 = E_0 \left(\frac{d}{r_1} \right) \exp \left(-j \frac{2\pi (r_1 - d)}{\lambda} \right), \quad (7)$$

while the electric field dE , that is measured at the RX node and generated by the area dS_N of the target N closest to the RX is given by

$$dE = j \frac{dE_N dS_N}{\lambda r_N} \exp \left(-j \frac{2\pi r_N}{\lambda} \right). \quad (8)$$

Combining Eqs. (6-8), it is

$$\begin{aligned} dE &= j^N \frac{d}{\lambda^N r_N r_{N-1,N} \dots r_{1,2} r_1} E_0 \cdot \\ &\cdot \exp \left\{ -j \frac{2\pi}{\lambda} (r_N + r_{N-1,N} + \dots + r_{1,2} + r_1 - d) \right\} \cdot \\ &\cdot dS_1 dS_2 \dots dS_N. \end{aligned} \quad (9)$$

To obtain the electric field E , Eq. (9) must be integrated over the domain $S^{(c)} = \bigcup_{n=1}^N S_n^{(c)}$ where each region $S_n^{(c)}$ corresponds to the 2D plane $\mathcal{P}_n \supset S_n$ that does not contain the points of the knife-edge surface S_n . Eq. (9) becomes now

$$\begin{aligned} \frac{E}{E_0} &= j^N \int_{S_1^{(c)}} \int_{S_2^{(c)}} \dots \int_{S_N^{(c)}} \frac{d}{\lambda^N r_N r_{N-1,N} \dots r_{1,2} r_1} \cdot \\ &\cdot \exp \left\{ -j \frac{2\pi}{\lambda} (r_N + r_{N-1,N} + \dots + r_{1,2} + r_1 - d) \right\} \cdot \\ &\cdot dS_1 dS_2 \dots dS_N. \end{aligned} \quad (10)$$

We now define $E^{(n)}$ as the value of the electric field at the RX node when only one target, *i.e.*, the n -th body or obstacle, is present in the LOS area. Similarly, $E^{(n,m)}$ refers to the electric field at the receiver when only the n -th and m -th obstacles out of N , are in the link area, and so on. The notation $E^{(1,2,\dots,N)}$ thus highlights the contributions of the N targets to the link loss: this is the total electric field E at the receiver given by (10). Considering the above definitions, Eq. (10) may be rewritten to highlight the mutual interactions of the targets, grouped by $\binom{N}{N-1}$ singles, $\binom{N}{N-2}$ pairs, $\binom{N}{N-3}$ triples and so on, as

$$\begin{aligned} (-1)^N \frac{E^{(1,2,\dots,N)}}{E_0} &= -1 + \underbrace{\sum_{n=1}^N \frac{E^{(n)}}{E_0}}_{\text{singles}} - \underbrace{\sum_{n=1}^{N-1} \sum_{m=n+1}^N \frac{E^{(n,m)}}{E_0}}_{\text{pairs}} + \\ &+ \underbrace{\sum_{n=1}^{N-2} \sum_{m=n+1}^{N-1} \sum_{k=m+1}^N \frac{E^{(n,m,k)}}{E_0}}_{\text{triples}} + \dots + \\ &+ \Psi(S_1, \dots, S_N) \end{aligned} \quad (11)$$

where the last term $\Psi(S_1, \dots, S_N)$:

$$\begin{aligned} \Psi(S_1, \dots, S_N) &= j^N \int_{S_1} \int_{S_2} \dots \int_{S_N} \frac{d}{\lambda^N r_N r_{N-1,N} \dots r_{1,2} r_1} \cdot \\ &\cdot \exp \left\{ -j \frac{2\pi}{\lambda} (r_N + r_{N-1,N} + \dots \right. \\ &\left. \dots + r_{1,2} + r_1 - d) \right\} \cdot dS_1 dS_2 \dots dS_N, \end{aligned} \quad (12)$$

is the integral computed over the composite domain defined by the union $S^{(1,2,\dots,N)} = \bigcup_{n=1}^N S_n$ of the N rectangular knife-edge surfaces S_n . The knife edge surfaces (Fig. 3) have the following definitions: for $n = 1$ it is $S_1 = \{(x, y, z) \in \mathbb{R}^3 : x = x_1 = d_1, y_1 - c_1/2 \leq y \leq y_1 + c_1/2, -H \leq z \leq h_1 - H\}$ while $\forall n = 2, \dots, N$ it is also $S_n = \{(x, y, z) \in \mathbb{R}^3 : x = x_n = d_1 + \sum_{i=1}^{n-1} d_{i,i+1}, y_n - c_n/2 \leq y \leq y_n + c_n/2, -H \leq z \leq h_n - H\}$.

Using (11), for a generic number of targets N , the electric field ratio $\frac{E^{(1,2,\dots,N)}}{E_0}$ due to N obstructing bodies is composed by the single target contributions $\frac{E^{(n)}}{E_0}$, for $n = 1, \dots, N$ terms, the target pairs, $\frac{E^{(n,m)}}{E_0}$, for $n = 1, \dots, N-1, m = n+1, \dots, N$, the triples, $\frac{E^{(n,m,k)}}{E_0}$, for $n = 1, \dots, N-2, m = n+1, \dots, N-1, k = m+1, \dots, N$, and so on, up to the contributions of the $N-1$ target groups. Likewise PSBM and SBM, MBM gives valid predictions when the targets are placed in the area \mathcal{V} near the LOS path, as defined in Sect. II-A.

When two bodies are in the area \mathcal{V} , the received electric field $E^{(1,2)}$ embeds the mutual effects of the two targets T_1 (*i.e.*, S_1) and T_2 (*i.e.*, S_2) on the radio propagation. $E^{(1,2)}$ is computed from the single-target terms $E^{(1)}$ and $E^{(2)}$ as

$$\frac{E^{(1,2)}}{E_0} = -1 + \frac{E^{(1)}}{E_0} + \frac{E^{(2)}}{E_0} + \Psi(S_1, S_2). \quad (13)$$

where the *mixed* term, that depends on both knife-edges S_1 and S_2 , is defined according to Eq. (12) as

$$\begin{aligned} \Psi(S_1, S_2) &= - \int_{S_1} \int_{S_2} \frac{d}{\lambda^2 r_2 r_{1,2} r_1} \cdot \\ &\cdot \exp \left\{ -j \frac{2\pi}{\lambda} (r_2 + r_{1,2} + r_1 - d) \right\} dS_1 dS_2. \end{aligned} \quad (14)$$

In particular, from Eq. (13), the term $E^{(1)}$ quantifies the effect of the target T_1 alone in the link area according to Eq. (4). It depends on the corresponding target size c_1 , the target height h_1 , the link height H from the floor, and the distances d_1

and $d - d_1 = d_2 + d_{12}$ of the body T_1 from the TX and RX, respectively. Likewise, $E^{(2)}$ refers to the contributions of target T_2 only, according to its target size c_2 and height h_2 , the link height H from the floor, and the distances $d_1 + d_{12}$ and d_2 of the body T_2 from the TX and RX, respectively.

For $N = 1$, the proposed multi-body model (MBM) reduces to the single body model (SBM) as expected since all singles, pairs, triples and other high order terms of Eq. (11) vanish except for the term $\Psi(S_1)$. The MBM model for $N = 2$ targets (13) has been initially introduced in [45] along with some preliminary results. This dual-target model can be directly obtained from the Eq. (10) or, equivalently, Eq. (11). Model comparisons are presented in Sect. IV.

D. Paraxial multi-body model (PMBM)

For HPS applications, paraxial hypotheses are realistic only for small target(s), namely for small enough c_i and h_i w.r.t. the path length d . The approximation also requires the subject to move nearby the LOS path, with small enough y_i and z_i , or located in the central part of the LOS path. Carrier wavelength λ is also much smaller than the distances x_i and $d - x_i$ (Sect. II-B). Since the paraxial approximation is useful in several applications, mostly outdoor, in the following section, we will approximate the full Eqs. (10) or (11) using paraxial assumptions. Such a model will be labeled as PMBM (Paraxial MBM).

Based on the paraxial approximation, Eq. (10) becomes

$$\begin{aligned} \frac{E}{E_0} = & \left(\frac{j}{2}\right)^N \int_{S_1^{(c)}} \int_{S_2^{(c)}} \cdots \int_{S_N^{(c)}} \\ & \frac{d d_{1,2} d_{2,3} \cdots d_{N-1,N}}{(d_1 + d_{1,2})(d_{1,2} + d_{2,3}) \cdots (d_{N-1,N} + d_N)} \cdot \\ & \cdot \exp \left\{ -j \frac{\pi}{2} (u_1^2 + u_2^2 + \cdots + u_N^2 - 2\alpha_{1,2} u_1 u_2 + \right. \\ & \left. - 2\alpha_{N-1,N} u_{N-1} u_N) \right\} du_1 du_2 \cdots du_N \cdot \\ & \cdot \exp \left\{ -j \frac{\pi}{2} (v_1^2 + v_2^2 + \cdots + v_N^2 - 2\alpha_{1,2} v_1 v_2 + \right. \\ & \left. - 2\alpha_{N-1,N} v_{N-1} v_N) \right\} dv_1 dv_2 \cdots dv_N. \end{aligned} \quad (15)$$

In the Appendix V, we show how to rewrite Eq. (15) to reveal the mutual interactions of targets as in Eq. (11).

For the case of $N = 2$ targets, Eq. (15) becomes now analytically tractable. Using the formulation shown in Eq. (13), adapted in Appendix V for paraxial assumptions, it is

$$\begin{aligned} \frac{E^{(1,2)}}{E_0} = & -1 + \frac{E^{(1)}}{E_0} + \frac{E^{(2)}}{E_0} - \frac{1}{4} \frac{d d_{1,2}}{(d_1 + d_{1,2})(d_{1,2} + d_2)} \cdot \\ & \cdot \int_{-\sqrt{2}H/R_1}^{+\sqrt{2}(h_1-H)/R_1} \int_{-\sqrt{2}H/R_2}^{+\sqrt{2}(h_2-H)/R_2} \\ & \exp \left\{ -j \frac{\pi}{2} (u_1^2 + u_2^2 - 2\alpha_{1,2} u_1 u_2) \right\} du_1 du_2 \cdot \\ & \cdot \int_{(\sqrt{2}y_1 - c_1/\sqrt{2})/R_1}^{(\sqrt{2}y_1 + c_1/\sqrt{2})/R_1} \int_{(\sqrt{2}y_2 - c_2/\sqrt{2})/R_2}^{(\sqrt{2}y_2 + c_2/\sqrt{2})/R_2} \\ & \exp \left\{ -j \frac{\pi}{2} (v_1^2 + v_2^2 - 2\alpha_{1,2} v_1 v_2) \right\} dv_1 dv_2, \end{aligned} \quad (16)$$

where u_1, u_2, v_1, v_2 and the constant terms R_1, R_2 and $\alpha_{1,2}$ defined in the same Appendix V. Notice that, some approximated models are already available in the literature [24], [46] for the evaluation of the extra attenuation due to multiple semi-infinite knife-edge surfaces. These models can be obtained by using the paraxial approximation over the semi-infinite domains representing the targets (*i.e.*, unlike the *finite* target size assumption adopted here); they are typically effective in outdoor scenarios for the prediction of the propagation loss over non-regular terrain profiles. The interested reader can take a look at [26] (and references therein) for a brief discussion and comparisons.

E. Additive models

Based on the analysis of the previous sections, the term $|E^{(1,2,\dots,N)}/E_0|$ for N targets can be used to evaluate the extra attenuation $A_{\text{dB}}^{(1,2,\dots,N)}$ with respect to the free-space (*i.e.*, unobstructed or empty) scenario as

$$A_{\text{dB}}^{(1,2,\dots,N)} = -10 \log_{10} \left| E^{(1,2,\dots,N)}/E_0 \right|^2. \quad (17)$$

From Eq. (11), it is apparent that the extra attenuation terms $\left| \frac{E^{(1)}}{E_0} \right|, \left| \frac{E^{(2)}}{E_0} \right|, \dots, \left| \frac{E^{(N)}}{E_0} \right|$ alone or, equivalently, $A_{\text{dB}}^{(1)}, A_{\text{dB}}^{(2)}, \dots, A_{\text{dB}}^{(N)}$, are not sufficient to evaluate $\left| \frac{E^{(1,2,\dots,N)}}{E_0} \right|$ since: *i*) the phase relations between the terms $\frac{E^{(n)}}{E_0}$ are unknown, *ii*) the terms $\frac{E^{(n,m)}}{E_0}, \frac{E^{(n,m,k)}}{E_0}, \dots$, are not available, and *iii*) the interaction terms between the targets, that are expressed by the integral of the right side of Eq. (11), are not known as well. These facts prevent the use of single-target measurements for the multiple target case. According to these considerations, the additive hypothesis, namely $A_{\text{dB}}^{(1,2,\dots,N)} = A_{\text{dB}}^{(1)} + A_{\text{dB}}^{(2)} + \dots + A_{\text{dB}}^{(N)}$, that is generally exploited in various forms in the literature [7], [17], is a rather superficial approximation. For the case of two targets ($N = 2$), in Sect. IV-C an additive SBM model is proposed where the individual extra attenuations $A_{\text{dB}}^{(1)}, A_{\text{dB}}^{(2)}, \dots, A_{\text{dB}}^{(N)}$ follow the SBM model described in Eq. (4). Limitations of such representation are highlighted by a comparison with the MBM and PMBM models.

III. PHYSICAL-STATISTICAL MULTI-BODY MODEL

In this section, we propose a true multi-target physical-statistical model that relates the RSS to the link geometry (d, H), the bodies locations \mathbf{X} , and their geometrical sizes (*i.e.*, \mathbf{a} , \mathbf{b} and \mathbf{h}). In addition to the diffraction, or physical, component analyzed in Sect. II, the additional statistical component quantifies the uncertainty of body movements, modelled here by small random voluntary/involuntary motions $\Delta \mathbf{X}$ and rotations χ around the nominal position \mathbf{X} , as well as multipath fading, multiple scattering between bodies, backward propagation effects, and other random fluctuations, not included in the diffraction terms. For the sake of simplicity, in the following sections, all geometrical parameters defined in Sect. II-C will be represented by the compact set $\Lambda = \{\mathbf{a}, \mathbf{b}, \mathbf{h}, d, H\}$.

Let P be the RSS measurement performed by the receiver RX and expressed in logarithmic scale (*i.e.*, usually in dBm),

the power measurement P can be modeled as the sum of *i*) the deterministic term $P_L = 10 \log_{10} |E_0|^2$ due to the free-space path-loss; *ii*) the extra attenuation term $A_{\text{dB}} = A_{\text{dB}}^{(1,2,\dots,N)}$ in (17) with respect to the free-space path-loss, caused by the body-induced diffraction terms, and *iii*) the Gaussian random term w that includes the lognormal multipath effects [56], measurement noise and other random disturbances assumed normally distributed. According to these assumptions, it is

$$P = \begin{cases} P_L - A_{\text{dB}}^{(1,2,\dots,N)} + w & \text{iff } \exists \mathbf{X}_n \in \mathcal{Y} \\ P_L + w_0 & \text{elsewhere.} \end{cases} \quad (18)$$

The free-space term P_L is a constant that depends only on the geometry of the scenario, the transmitted power, the gain and configuration of the antennas, and the propagation coefficients [50]. The term $A_{\text{dB}}^{(1,2,\dots,N)} = A_{\text{dB}}(\mathbf{X}, \Delta\mathbf{X}, \chi, \Lambda)$ is the extra attenuation, expressed in dB, due to the body-induced diffraction with respect to the free-space scenario. Its argument $|E^{(1,2,\dots,N)}|/|E_0|^2$ is computed using (10) or (11) for MBM and (15) or (23) for PMBM. Propagation effects not included in the diffraction models (10) or (11) are modeled by the Gaussian noise $w \sim \mathcal{N}(\Delta\mu_C, \sigma_0^2 + \Delta\sigma_C^2)$ with $\Delta\mu_C$ and $\Delta\sigma_C^2$ being the residual stochastic body-induced multipath fading mean and variance terms [49], [55]. σ_0^2 models the power fluctuations induced by environmental changes outside the link area, and not attributable to body movements around the LOS link.

For the empty scenario, where nobody is present in the link area, namely the *background* configuration, the RSS is simply modelled as $P = P_L + w_0$ with $w_0 \sim \mathcal{N}(0, \sigma_0^2)$. Notice that in HPS systems, $\mu_0 = E_{w_0}[P] = P_L$ and $\sigma_0^2 = \text{Var}_{w_0}[P]$ can be evaluated from field measurements during a calibration phase, when there are no targets in the link area. On the contrary, the presence of people modifies both the mean $\mu_1(\mathbf{X}) = E_{\chi, \Delta\mathbf{X}, w}[P]$ and the variance $\sigma_1^2(\mathbf{X}) = \text{Var}_{\chi, \Delta\mathbf{X}, w}[P]$ terms. Based on Eq. (18), the mean $\mu(P)$ and variance $\sigma^2(P)$ are defined as

$$\mu(P) = \begin{cases} \mu_1(\mathbf{X}|\Lambda) = P_L + \Delta\mu(\mathbf{X}|\Lambda) & \text{iff } \exists \mathbf{X}_n \in \mathcal{Y} \\ \mu_0 = P_L & \text{elsewhere} \end{cases} \quad (19)$$

and

$$\sigma^2(P) = \begin{cases} \sigma_1^2(\mathbf{X}|\Lambda) = \sigma_0^2 + \Delta\sigma^2(\mathbf{X}|\Lambda) & \text{iff } \exists \mathbf{X}_n \in \mathcal{Y} \\ \sigma_0^2 & \text{elsewhere} \end{cases} \quad (20)$$

where it is emphasized the dependency of P from the position \mathbf{X}_n of at least one target T_n in the area \mathcal{Y} and the geometrical coefficients Λ . The RSS average $\Delta\mu(\mathbf{X}) = \mu_1(\mathbf{X}) - \mu_0$ and variance $\Delta\sigma^2(\mathbf{X}) = \sigma_1^2(\mathbf{X}) - \sigma_0^2$ increments are defined as

$$\Delta\mu(\mathbf{X}|\Lambda) = \Delta\mu_C - E_{\chi, \Delta\mathbf{X}}[A_{\text{dB}}(\mathbf{X}|\Delta\mathbf{X}, \chi, \Lambda)] \quad (21)$$

and

$$\Delta\sigma^2(\mathbf{X}|\Lambda) = \Delta\sigma_C^2 + \text{Var}_{\chi, \Delta\mathbf{X}}[A_{\text{dB}}(\mathbf{X}|\Delta\mathbf{X}, \chi, \Lambda)] . \quad (22)$$

The term $A_{\text{dB}}(\mathbf{X}|\Delta\mathbf{X}, \chi, \Lambda)$ highlights the fact that, given the geometrical parameters Λ and the motion terms $\Delta\mathbf{X}$, χ ,

the extra attenuation is only a function of the positions \mathbf{X} of the bodies. In the followings, we assume that the bodies are positioned in \mathbf{X} but each of them can slightly change its location and posture making small random movements $\Delta\mathbf{X}_n$ with $\Delta x_n, \Delta y_n \sim \mathcal{U}(-B, +B)$ and rotations $\chi_n \sim \mathcal{U}(-\pi, +\pi)$ around the vertical axis. $\mathcal{U}(\alpha, \beta)$ indicates the uniform distribution within the interval $[\alpha, \beta]$ while, for each n , the set $[-B, +B] \times [-B, +B]$ defines the 2D area around the nominal coordinate position \mathbf{X}_n where the n -th target can freely move. To determine eqs. (21) and (22), the mean $E_{\chi, \Delta\mathbf{X}}[\cdot]$ and the variance $\text{Var}_{\chi, \Delta\mathbf{X}}[\cdot]$ are computed over the aforementioned uniform distribution of $\Delta\mathbf{X}$ and χ .

The residual body-induced multipath terms $\Delta\mu_C$ and $\Delta\sigma_C^2$ in (21) and (22), respectively, can be directly evaluated from field measurements performed during the calibration phase. However, these terms are marginally influenced by the specific body locations, as also shown in [49], [56], and are thus not relevant for HPS applications. On the contrary, the diffraction term $A_{\text{dB}}(\mathbf{X}|\Delta\mathbf{X}, \chi, \Lambda)$ provides a simple but effective method to predict the power perturbation $\Delta\mu(\mathbf{X}|\Lambda)$ and $\Delta\sigma^2(\mathbf{X}|\Lambda)$ as a function of the body position and size.

IV. MODEL OPTIMIZATION AND VALIDATION

To confirm the validity of the proposed multi-body models, several EM simulations with the Feko software environment and on-field experiments have been carried out according to the same link scenario sketched in Fig. 3. Feko¹ implements time and frequency domain full-wave solvers (*e.g.*, MoM, FDTD, FEM and MLFMM). For details about the solvers, the interested reader may have a look at [57].

First of all, simulations have been carried out to compare the results of the diffraction-based MBM and PMBM models shown in Sect. II-C and Sect. II-D, respectively, with the ones obtained with Feko. Next, we have compared the aforementioned models against the RSS measurements obtained from IEEE 802.15.4 devices [58], commonly used in industrial applications [59]. Considering the application to multi-body localization featuring $N = 2$ targets, the MBM and PMBM model parameters, namely the geometrical sizes (*i.e.*, \mathbf{a} , \mathbf{b} and \mathbf{h}) of the knife-edge surfaces, are optimized using a small subset of the experimental data so that they could effectively model the obstructions induced by the true targets. The proposed models using optimized sizes of the knife-edges are then validated over different configurations, where both targets move along the LOS link.

It is worth noticing that Feko simulations are related to PEC (Perfect Electromagnetic Conductor) configurations to describe knife-edge targets. On the contrary, MBM and PMBM 2D models assume perfectly absorbing surfaces. The MBM and PMBM models also ignore important EM parameters such as polarization, permittivity, conductivity, shape, radius of curvature, and surface roughness [53] that the Feko simulator is able to tackle.

¹The commercial EM simulator designed by Altair Engineering Inc.

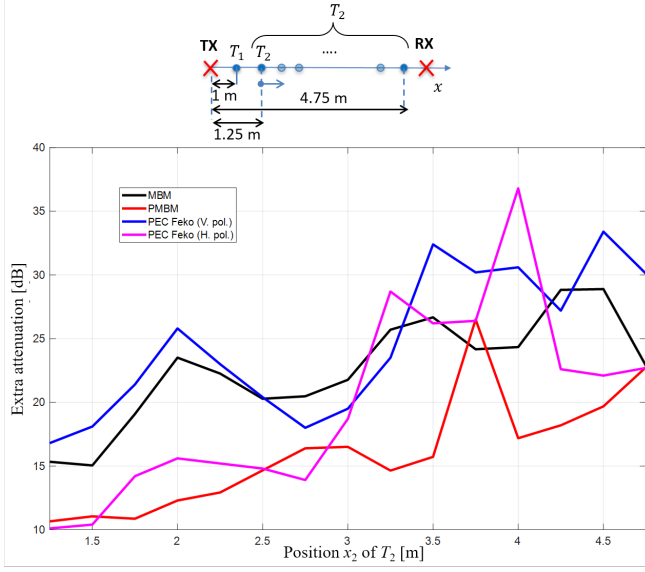


Figure 4. Feko PEC simulations for vertically (blue line) and horizontally (magenta line) polarized source vs. MBM (black line) and PMBM (red line) $A_{\text{dB}}^{(1,2)}$ predictions for targets T_1 and T_2 along the LOS path as shown in the scenario on the top.

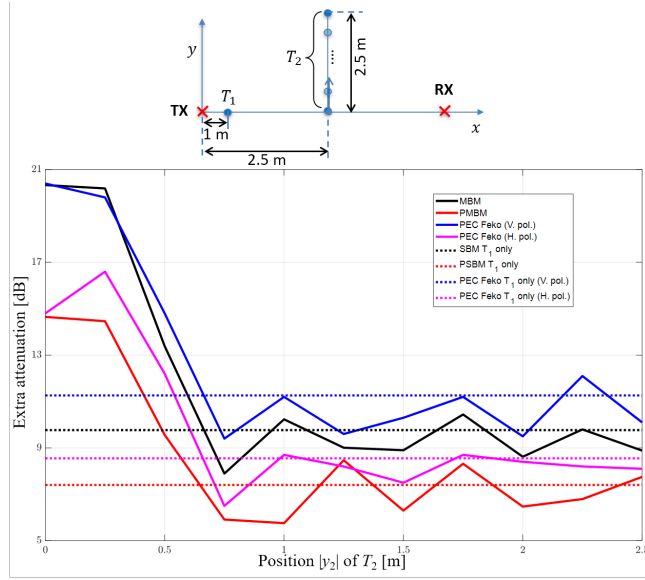


Figure 5. Feko PEC simulations for vertically (blue line) and horizontally (magenta line) polarized source vs. MBM (black line) and PMBM (red line) $A_{\text{dB}}^{(1,2)}$ predictions for the target T_1 along the LOS path and T_2 across the LOS path as shown in the scenario on the top. The dotted lines (with the same colors adopted for the dual-target cases) show the extra attenuation predicted by the previous models/simulations due to the presence of the target T_1 only.

A. Model comparison against EM simulations

The MBM and PMBM models are evaluated and compared in this section with the results from EM simulations. To simplify the EM simulation complexity (mostly due to the long Feko runs), in what follows MBM and PMBM models are compared in a dual-target scenario ($N = 2$) only. Fig. 4 and 5 show the predicted values of the extra attenuation $A_{\text{dB}}^{(1,2)} = -10 \log_{10} |E^{(1,2)}/E_0|^2$ computed according to the models described by eqs. (13) and (16), namely MBM and PMBM, respectively. No movements/rotations are allowed and

Table I
AVERAGE ERRORS AND STANDARD DEVIATION VALUES IN THE LOS AREA OBTAINED BY MBM AND PMBM PREDICTIONS *w.r.t.* FEKO PEC V. POL. SIMULATIONS.

LOS area	ϵ_{MBM}	σ_{MBM}	ϵ_{PMBM}	σ_{PMBM}
Along (Fig. 4)	-2.1 dB	3.4 dB	-8.7 dB	4.4 dB
Across (Fig. 5)	-1.0 dB	0.7 dB	-4.0 dB	1.5 dB

both targets are placed in their nominal positions: in both figures, the target T_1 is fixed in the position $\mathbf{X}_1 = [1, 0]^T$ while the target T_2 changes its positions along and across the LOS path. In Fig. 4, T_2 is placed in $\mathbf{X}_2 = [x_2, 0]^T$ and moves along the LOS path with $1 < x_2 < d$ and 0.25 m increments while in Fig. 5 the target T_2 is placed in $\mathbf{X}_2 = [d/2, y_2]^T$ with $-2.5 < y_2 < 2.5$ m and 0.25 m increments thus crossing the LOS path in the middle. For symmetry reasons, the results depends only on the distance $|y_2|$ from the LOS line.

In these figures, we compare the results of the MBM and PMBM against the ones of the EM simulations obtained with Feko using vertically and horizontally polarized sources (*i.e.*, Feko V. pol. and H. pol., respectively). For these simulations, a 2D PEC surface have been used as target instead of the absorbing one defined in Sect. II for MBM and PMBM, but with the same physical dimensions adopted for Fig. 1. Target T_1 and T_2 have the same size $c_1 = c_2 = 0.55$ m and height $h_1 = h_2 = 1.80$ m while $H = 0.90$ m and $d = 5.0$ m. The average error ϵ_{MBM} (and ϵ_{PMBM}) between MBM (and PMBM) and Feko PEC V. pol. values in dB are summarized in Tab. I, where the corresponding standard deviation values σ_{MBM} (and σ_{PMBM}) are also included. The sign in the average errors ϵ_{MBM} and ϵ_{PMBM} indicates that the results of the MBM and PMBM models underestimate in average the Feko results.

Along the LOS positions of Fig. 4, the average errors are $\epsilon_{\text{MBM}} = -2.1$ dB and $\epsilon_{\text{PMBM}} = -8.7$ dB, respectively, while the corresponding standard deviations are $\sigma_{\text{MBM}} = 3.4$ dB and $\sigma_{\text{PMBM}} = 4.4$ dB, as well. As already noted, while the MBM trend is similar to the one due to the Feko predictions, the PMBM values introduce too many large errors. These effects are also apparent in Fig. 5 where the target T_2 move along the orthogonal line that crosses the LOS in the middle at $x_2 = 2.5$ m. Even in this case, the MBM trend is similar to the PEC vertical polarized curve predicted by the Feko software with an maximum error in the order of $1 \div 2$ dB. In particular, $\epsilon_{\text{MBM}} = -1.0$ dB, $\epsilon_{\text{PMBM}} = -4.0$ dB, $\sigma_{\text{MBM}} = 0.7$ dB and $\sigma_{\text{PMBM}} = 1.5$ dB considering all positions across the LOS line. In Fig. 5, the results corresponding to the models for the single target T_1 are superimposed to the ones predicted by the MBM/PMBM models and the ones obtained with Feko. When target T_2 moves away from the LOS path the effects due to this target vanish, while the extra attenuation can be well predicted using only the single target body model for T_1 . The difference between the values predicted by the MBM (and PMBM) model and the Feko simulations are due to the fact that the former employs absorbing targets and neglects any polarization while the latter exploits metallic plates and includes the polarization effects. The positions with larger differences (*i.e.*, up to $5 \div 6$ dB) are visible in the right part

of Fig. 4 where the target T_2 is very close to the receiver and the metallic nature of the PEC is more evident. Even if some positions of Fig. 4 show some relevant differences between MBM and Feko results, the general trend is maintained. On the contrary, differences between the MBM (and PMBM) model and the Feko simulations are smaller for off-axis placement of T_2 as shown in Fig. 5. It is also worth noticing in Fig. 4 the strong differences between vertically and horizontally polarized results obtained with Feko.

B. Model optimization and experiments

Localization, and, in general, HPS systems, rely on several calibration steps that include off-line measurements stages to collect ground-truth measurements of radio propagation. Detection algorithms based on finger-printing approaches [6] require also the presence of the target(s) in known locations, namely landmark points, to perform RF measurements with target(s) inside the monitored area. These steps are very time consuming and error-prone since each RF node needs to perform noisy RSS signal measurements for the assessment of body-induced alterations of the radio propagation with the target(s) placed in the selected landmarks (*i.e.*, 2-4 landmarks/sqm depending on the network placement). In addition, systematic errors can be also introduced in the experimental setup during target positioning. Moreover, modifications of the environment involve frequent recalibration steps to maintain a good level of localization accuracy. In what follows, we investigate the use of the multi-body models of Sect. III optimized to replace, or simplify, such calibration phases.

Model optimization, or tuning, is implemented during an initial stage to estimate the MBM and PMBM model hyperparameters, the geometrical sizes \mathbf{a} , \mathbf{b} and \mathbf{h} . We thus collect a small set of measurements in selected landmark points: these are used to tune both MBM and PMBM physical parameters, namely the *EM-equivalent* height h_n and width $c_n \in [a_n, b_n]$ of the n -th deployed subject. Using these optimized hyperparameters, the MBM and the PMBM representations can be finally adopted to predict body effects at arbitrary positions, replacing conventional calibration stages [6].

RSS data have been collected in a large hall by using two IEEE 802.15.4-compliant radio devices, based on the NXP JN5148 SoC (System-on-Chip) [60], that are employed as transceiver (TX/RX) nodes. Link geometry is $H = 0.9$ m and $d = 5$ m for all cases. Each device is equipped with 2 dBi vertical monopole antennas and is programmed to send IEEE 802.15.4 standard frames at frequency $f_c = 2.486$ GHz (corresponding to IEEE 802.15.4 channel 26 [58]). The receiver decodes each frame to extract a measurement of RSS, namely the digital RSS Indicator (RSSI) with 8-bit resolution [61] and 1 dB quantization. Two set of measurements have been gathered: the first dataset, acquired in the empty scenario, has been used to compute the reference values μ_0 and σ_0^2 , while the second one has been recorded with two targets are placed in the link area and move concurrently. The second data set has been used to measure $\mu_1(\mathbf{X})$ and $\sigma_1^2(\mathbf{X})$ for some known landscape positions \mathbf{X} . In particular, the subject T_1 was placed at $\mathbf{X}_1 = [2.5, 0]^T$ from the transmitter, the second

subject T_2 covered 4 different positions, $\mathbf{X}_2 = [x_2, 0]^T$, at distances $x_2 = 3$ m, $x_2 = 3.5$ m, $x_2 = 4$ m and $x_2 = 4.5$ m, respectively. These locations have been used to optimize the EM-equivalent geometrical dimensions c_1, c_2, h_1, h_2 of the individual subjects using a Non-linear Least Squares (NLS) approach as in [62]. The optimization is iterative and uses the nominal (or physical) size of the targets as initial inputs, namely $c_1 = c_2 = 0.4$ m and $h_1 = h_2 = 1.7$ m (neglecting head). Optimized EM-equivalent target size are $c_1 = c_2 = 0.25$ m and $h_1 = h_2 = 1.35$ m. The EM-equivalent size is about 20% ÷ 40% smaller than the physical size of the target as also shown in [35]: this might be due to the fact that body-induced extra attenuations are mostly due to torso and legs, while the effects caused by head and arms are negligible, although they are responsible for some small RSSI fluctuations.

C. Model comparison with measurements

Based on the experimental set-up described in the previous section, we compare in Fig. 6 the predicted extra attenuation $E_{\mathbf{X}, \Delta \mathbf{X}} [A_{\text{dB}}^{(1,2)}(\mathbf{X} | \Delta \mathbf{X}, \boldsymbol{\chi}, \boldsymbol{\Lambda})]$ using the MBM (black line) and PMBM (blue line) models against the field measurements (red cross). RSSI measurements, averaged over a period of 1 minute, are indicated in Fig. 6 as red cross markers. Horizontal error bars are also depicted to account for positioning inaccuracies (± 0.25 m) during the tests while vertical bars and dots indicate the max-min and mean RSSI values, respectively. Solid lines show the predicted MBM and PMBM extra attenuations using the optimized EM-equivalent parameters. For prediction, we consider two knife-edges placed along the LOS path in fixed positions ($B = 0$) with no rotation. In particular, subject T_1 initially placed at $\mathbf{X}_1 = [0.5, 0]^T$ from the transmitter covers a distance of 1.5 m in the direction of the RX (thus stopping at $\mathbf{X}_1 = [2, 0]^T$ from the TX). Subject T_2 moves towards the receiver and stops at 0.5 m from the device.

To highlight the comparative analysis with measurements, we neglect the residual stochastic body-induced multipath fading terms by assuming $\Delta\sigma_C^2 = 0$ dB and $\Delta h_C = 0$ dB, so that Eq. (21) reduces to $-\Delta\mu(\mathbf{X}) = E_{\mathbf{X}, \Delta \mathbf{X}} [A_{\text{dB}}^{(1,2)}(\mathbf{X} | \Delta \mathbf{X}, \boldsymbol{\chi}, \boldsymbol{\Lambda})] = A_{\text{dB}}^{(1,2)}(\mathbf{X} | \boldsymbol{\Lambda})$. Besides MBM and PMBM models, based on the discussion in Sect. II-E, for the same settings, we have also compared the additive hypothesis, namely $A_{\text{dB}}^{(1,2)} = A_{\text{dB}}^{(1)} + A_{\text{dB}}^{(2)}$. In particular, the additive SBM approximation is depicted in dashed lines: in this case, the predicted extra attenuation reduces to $-\Delta\mu(\mathbf{X}) = E_{\mathbf{X}_1, \Delta \mathbf{X}_1} [A_{\text{dB}}^{(1)}(\mathbf{X} | \Delta \mathbf{X}, \boldsymbol{\chi}, \boldsymbol{\Lambda})] + E_{\mathbf{X}_2, \Delta \mathbf{X}_2} [A_{\text{dB}}^{(2)}(\mathbf{X} | \Delta \mathbf{X}, \boldsymbol{\chi}, \boldsymbol{\Lambda})] = A_{\text{dB}}^{(1)}(\mathbf{X} | \boldsymbol{\Lambda}) + A_{\text{dB}}^{(2)}(\mathbf{X} | \boldsymbol{\Lambda})$ where $A_{\text{dB}}^{(1)}(\mathbf{X} | \boldsymbol{\Lambda})$ and $A_{\text{dB}}^{(2)}(\mathbf{X} | \boldsymbol{\Lambda})$ follow the SBM model described in Sect. II-A and use the same optimized EM-equivalent target size as that of the MBM model.

In Fig. 6, the shaded areas indicate the ± 1 dB uncertainty zone around the mean values predicted by the MBM (*i.e.*, beige area) and the additive SBM (*i.e.*, light blue area) models. Assuming Gaussian distributions, for each uncertainty zone, the 68.3% of the related events fall inside each shaded area.

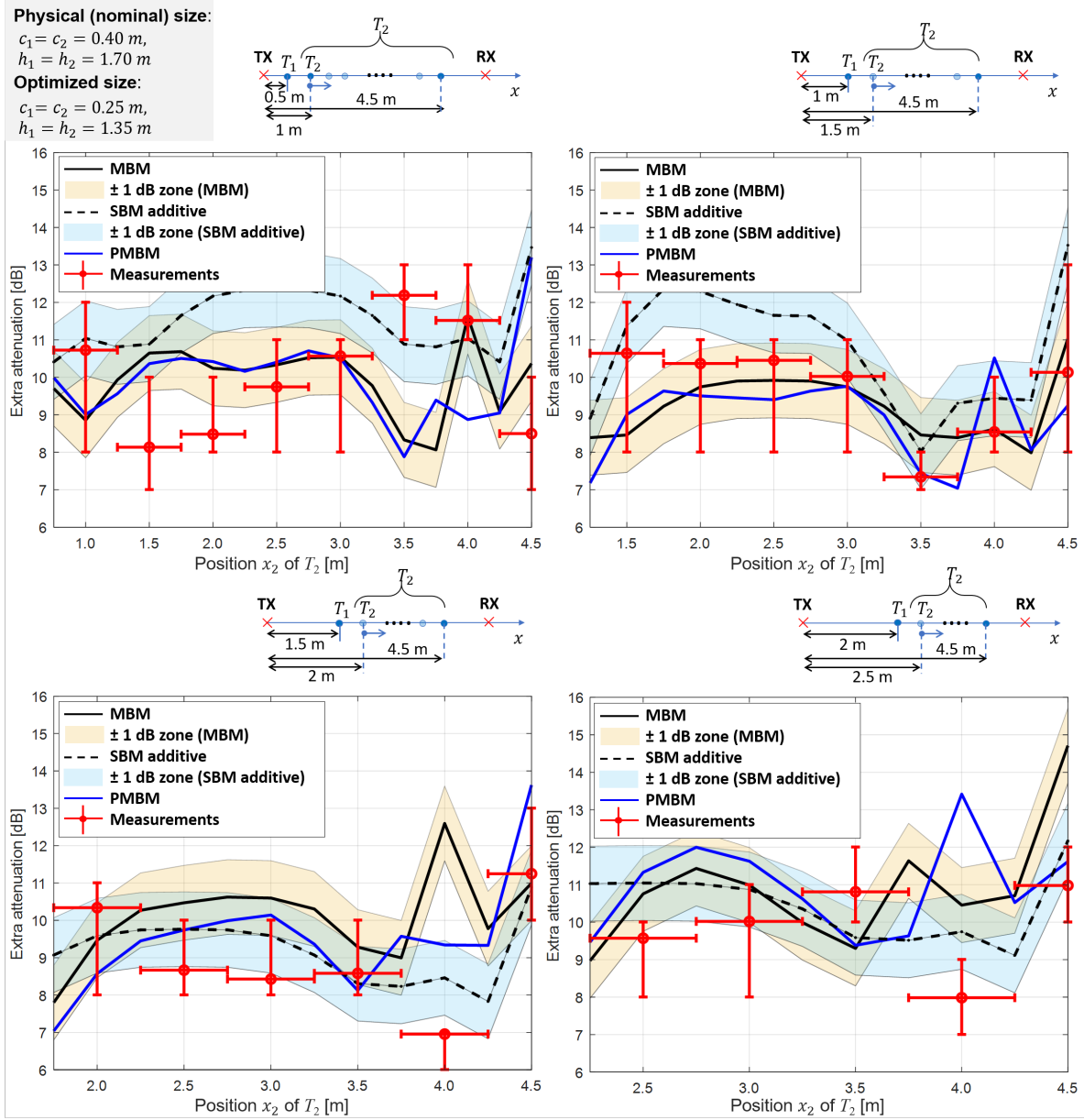


Figure 6. Predicted extra attenuation values using MBM (black line), PMBM (blue line) and additive SBM (black dashed line) against the measured ones (red cross, with vertical and horizontal error bars) considering 4 motion scenarios featuring $N = 2$ targets. The ± 1 dB uncertainty zones are shown around the additive SBM (light blue area) and the MBM (beige area) results. Each scenario is depicted in the corresponding sub-figure.

The discrepancies between the proposed models and the measurements may be large for some target positions, configurations and scenarios. This is due to some approximations adopted for the MBM/PMBM and SBM/PSBM models that are summarized here: *i*) the diffraction models assume a 2D knife-edge approximation to describe each 3D target. In addition, each knife-edge surface is assumed to be completely absorbing [43] while this is just an approximation for the human body [39]; *ii*) the multi-body diffraction model derived here assumes only forward propagation from the transmitter to the receiver and ignores reverberations among targets; *iii*) the diffraction model, being based on the scalar diffraction theory, does not include polarization effects; *iv*) the EM composition of the targets is not considered.

In addition, there are also some noisy effects during the

RSS measurement: *v*) the human bodies are never fixed in specific positions but, while standing, they have both voluntary and/or involuntary movements around the nominal position due to movements of the legs, torso, arms and head. This experimental fact can introduce variations in the order of $2 \div 3$ dB for the single target case [43]; *vi*) due to the complex structure of the human body and the difficulties to measure the true position of the body [43], [62], the nominal (measured) position of the target is only approximately known (with an error in the order of $10 \div 15$ cm); *vii*) the measurements are taken in real scenarios where some multipath effects are present. These effects are modeled as a lognormal distributed noise even if this is an approximated behavior [56]; *viii*) the RSS values measured by the IEEE 802.15.4 radio devices are corrupted by measurement noise and non-linearity effects [61]

in the order of $0.5 \div 1.5$ dB, depending on the adopted device. Offset errors can be compensated due to the fact that the extra attenuation is measured *w.r.t.* the free-space scenarios but non-linearity and quantization cannot. Moreover, the radios are subject to some other artifacts since, at very low RSSI, namely when more than one target is near the LOS path, some packets are lost due to body shadowing effects [49], [55]; these target configurations introduce some high attenuated RSSI samples, mainly near the RX or the TX.

In Fig. 6, the MBM and PMBM predictions track the average RSSI measurements with an average error of about 4 dB and 6 dB, respectively. Notice that most of the mismatches between the models and the measurements are observed in correspondence to one of the targets (or both) near the transmitter or the receiver. In such cases, the RSSI measurements might be also affected by larger communication errors due to the increase of body-induced extra attenuation. Fluctuations of RSSI around the average value cause residual stochastic terms that can be quantified as a variance term $\Delta\sigma_C^2 \simeq 3$ dB and negligible mean $\Delta h_C \simeq 0$ dB: these are mostly due to voluntary/involuntary movements of the bodies around their nominal positions. The additive SBM model is generally less effective compared with MBM, particularly when the mixed terms in Eq. (14), caused by the interacting targets T_1 and T_2 , could not be neglected. This is for example the case when both subjects equally contribute to the extra attenuation, *i.e.*, for subject T_1 placed at 0.5 m, $\mathbf{X}_1 = [0.5, 0]^T$, and 1 m, $\mathbf{X}_1 = [1, 0]^T$, from the transmitter.

V. CONCLUSIONS

Based on the electromagnetic (EM) scalar diffraction theory, the paper proposes for the first time an ad-hoc physical-statistical model to describe the fluctuations of the radio signal caused by the presence of an arbitrary number of targets between the transmitter and receiver. The analytical model has been specifically tuned and optimized to predict the effects of multiple bodies placed near the link area. Therefore, it is instrumental to Device-Free Localization (DFL) applications and Human Presence-aware Systems (HPS), including people access monitoring and counting. The model results have been validated experimentally by some field tests using real industrial wireless devices and EM simulations as well, for comparative analysis. The proposed multi-body model is able to predict the Received Signal Strength (RSS) measurements accounting for the size, orientation, small movements, and positions of the targets. In addition, it overcomes some restrictions of the existing multi-body models, based on the linear superposition of the subject effects, thus showing improved prediction accuracy.

APPENDIX

In what follows, we resort to a formulation of Eq. (15) similar to that used in Eq. (11). It is

$$(-1)^N \frac{E^{(1,2,\dots,N)}}{E_0} = -1 + \sum_{n=1}^N \frac{E^{(n)}}{E_0} - \sum_{n=1}^{N-1} \sum_{m=n+1}^N \frac{E^{(n,m)}}{E_0} + \sum_{n=1}^{N-2} \sum_{m=n+1}^{N-1} \sum_{k=m+1}^N \frac{E^{(n,m,k)}}{E_0} + \dots + \tilde{\Psi}(S_1, \dots, S_N) \quad (23)$$

with last term $\tilde{\Psi}(S_1, \dots, S_N)$:

$$\tilde{\Psi}(S_1, \dots, S_N) = \left(\frac{j}{2}\right)^N \int_{S_1} \int_{S_2} \dots \int_{S_N} \frac{d d_{1,2} d_{2,3} \dots d_{N-1,N}}{(d_1 + d_{1,2})(d_{1,2} + d_{2,3}) \dots (d_{N-1,N} + d_N)} \cdot \exp \left\{ -j \frac{\pi}{2} (u_1^2 + u_2^2 + \dots + u_N^2 - 2\alpha_{1,2} u_1 u_2 \dots + 2\alpha_{N-1,N} u_{N-1} u_N) \right\} du_1 du_2 \dots du_N \cdot \exp \left\{ -j \frac{\pi}{2} (v_1^2 + v_2^2 + \dots + v_N^2 - 2\alpha_{1,2} v_1 v_2 \dots + 2\alpha_{N-1,N} v_{N-1} v_N) \right\} dv_1 dv_2 \dots dv_N. \quad (24)$$

The variables $u_1, \dots, u_N, v_1, \dots, v_N$ are obtained from the corresponding local coordinates $\xi_1, \dots, \xi_N, \varsigma_1, \dots, \varsigma_N$ by using, for each n -th term, the following substitution rules: $u_n = \xi_n \frac{\sqrt{2}}{R_n}$ and $v_n = \varsigma_n \frac{\sqrt{2}}{R_n}$. The constant terms R_n and $\alpha_{n,n+1}$ are related to the wavelength λ and the geometric positions of the knife-edges with respect to the LOS path. The terms R_n are similar to the Fresnel's radius R for the single-target case. These constants are given by

$$\frac{1}{R_n^2} = \begin{cases} \frac{1}{\lambda} \left(\frac{1}{d_1} + \frac{1}{d_{12}} \right) & \text{for } n = 1 \\ \frac{1}{\lambda} \left(\frac{1}{d_{n-1,n}} + \frac{1}{d_{n,n+1}} \right) & \text{for } n = 2, \dots, N-1 \\ \frac{1}{\lambda} \left(\frac{1}{d_N} + \frac{1}{d_{N-1,N}} \right) & \text{for } n = N \end{cases} \quad (25)$$

while coefficients $\alpha_{n,n+1}$ are defined, for $n = 1, \dots, N-1$, as

$$\alpha_{n,n+1} = \frac{R_n R_{n+1}}{\lambda d_{n,n+1}}. \quad (26)$$

For the single-target case, it is $R_1 = R$ while all coefficients $\alpha_{n,n+1}$ vanish. In addition, it is trivial to verify that Eq. (11) simply reduces to Eq. (4) while Eq. (23) simplifies to (5). For $N = 2$, Eq. (11) reduces to the dual-target case (13) and proves the results [8] applied for localization purposes.

REFERENCES

- [1] V. Petrov, K. Mikhaylov, D. Moltchanov, S. Andreev, G. Fodor, J. Torsner, H. Yanikomeroglu, M. Juntti, and Y. Koucheryavy, "When iot keeps people in the loop: A path towards a new global utility," *IEEE Communications Magazine*, vol. 57, no. 1, pp. 114–121, 2019.
- [2] N. Dalal and B. Triggs, "Histograms of oriented gradients for human detection," in *2005 IEEE Computer Society Conference on Computer Vision and Pattern Recognition (CVPR'05)*, vol. 1, Jun. 2005, pp. 886–893 vol. 1.

- [3] Y. Benezeth, H. Laurent, B. Emile, and C. Rosenberger, "Towards a sensor for detecting human presence and characterizing activity," *Energy and Buildings*, vol. 43, no. 2, pp. 305–314, 2011.
- [4] B. Choi, M. MeriÄšli, J. Biswas, and M. Veloso, "Fast human detection for indoor mobile robots using depth images," in *2013 IEEE International Conference on Robotics and Automation*, May 2013, pp. 1108–1113.
- [5] M. Youssef, M. Mah, and A. Agrawala, "Challenges: Device-free passive localization for wireless environments," in *Proceedings of the 13th Annual ACM International Conference on Mobile Computing and Networking (MobiCom '07)*. ACM, 2007, pp. 222–229.
- [6] S. Savazzi, S. Sigg, M. Nicoli, V. Rampa, S. Kianoush, and U. Spagnolini, "Device-free radio vision for assisted living: Leveraging wireless channel quality information for human sensing," *IEEE Signal Processing Magazine*, vol. 33, no. 2, pp. 45–58, 2016.
- [7] J. Wilson and N. Patwari, "Radio tomographic imaging with wireless networks," *IEEE Transactions on Mobile Computing*, vol. 9, no. 5, pp. 621–632, May 2010.
- [8] M. Nicoli, V. Rampa, S. Savazzi, and S. Schiaroli, "Device-free localization of multiple targets," in *Signal Processing Conference (EUSIPCO), 2016 24th European*. IEEE, 2016, pp. 738–742.
- [9] J. Wang, D. Fanf, Z. Yang, H. Jiang, X. Chen, T. Xing, and L. Cai, "E-hipa: An energy-efficient framework for high-precision multi-target-adaptive device-free localization," *IEEE Trans. on Mobile Computing*, vol. 16, no. 3, pp. 716–729, Mar. 2017.
- [10] S. Depatla, A. Muralidharan, and Y. Mostofi, "Occupancy estimation using only wifi power measurements," *IEEE Journal on Selected Areas in Communications*, vol. 33, no. 7, pp. 1253–1264, 2015.
- [11] S. Savazzi, S. Kianoush, and V. Rampa, "A dynamic bayesian network approach for device-free radio vision: Modeling, learning and inference for body motion recognition," in *Acoustics, Speech and Signal Processing (ICASSP), 2016 IEEE International Conference on*. IEEE, 2016, pp. 6265–6269.
- [12] W. Wang, A. X. Liu, M. Shahzad, K. Ling, and S. Lu, "Understanding and modeling of wifi signal based human activity recognition," in *Proceedings of the 21st annual international conference on mobile computing and networking*. ACM, 2015, pp. 65–76.
- [13] S. Kianoush, S. Savazzi, F. Vicentini, V. Rampa, and M. Giussani, "Device-free rf human body fall detection and localization in industrial workplaces," *IEEE Internet of Things Journal*, 2016.
- [14] Z. Talebpour and A. Martinoli, "Adaptive risk-based replanning for human-aware multi-robot task allocation with local perception," *IEEE Robotics and Automation Letters*, vol. 4, no. 4, pp. 3790–3797, 2019.
- [15] A. Montanari, S. Nawaz, C. Mascolo, and K. Sailer, "A study of bluetooth low energy performance for human proximity detection in the workplace," in *2017 IEEE International Conference on Pervasive Computing and Communications (PerCom)*. IEEE, 2017, pp. 1–10.
- [16] K. Woyach, D. Puccinelli, and M. Haenggi, "Sensorless sensing in wireless networks: Implementation and measurements," in *4th International Symposium on Modeling and Optimization in Mobile, Ad Hoc and Wireless Networks*, April 2006, pp. 1–8.
- [17] N. Patwari and J. Wilson, "RF Sensor Networks for Device-Free Localization: Measurements, Models, and Algorithms," *Proceedings of the IEEE*, vol. 98, no. 11, pp. 1961–1973, Nov. 2010.
- [18] M. Seifeldin, A. Saeed, A. Kosba, A. El-Keyi, and M. Youssef, "Nuzzer: A large-scale device-free passive localization system for wireless environments," *IEEE Transactions on Mobile Computing*, vol. 12, no. 7, pp. 1321–1334, July 2013.
- [19] A. Saeed, A. Kosba, and M. Youssef, "Ichnaea: A low-overhead robust wlan device-free passive localization system," *IEEE Journal of Selected Topics in Signal Processing*, vol. 8, no. 1, pp. 5–15, Feb. 2014.
- [20] S. Obayashi and J. Zander, "A body-shadowing model for indoor radio communication environments," *IEEE Transactions on Antennas and Propagation*, vol. 46, no. 6, pp. 920–927, 1998.
- [21] F. Villanese, N. E. Evans, and W. G. Scanlon, "Pedestrian-induced fading for indoor channels at 2.45, 5.7 and 62 ghz," in *Vehicular Technology Conference, 2000. IEEE-VTS Fall VTC 2000. 52nd*, vol. 1. IEEE, 2000, pp. 43–48.
- [22] J. E. Brittain, "Albert Hoyt Taylor [Scanning the Past]," *Proceedings of the IEEE*, vol. 82, no. 6, pp. 958–, June 1994.
- [23] K. Furutsu, "On the theory of radio wave propagation over inhomogeneous earth," *Journal of Research of the NBS-D, Radio Propagation*, vol. 67D, no. 1, pp. 39–62, Jan.-Feb. 1963.
- [24] L. Vogler, "An attenuation function for multiple knife-edge diffraction," *Radio Science*, vol. 17, no. 06, pp. 1541–1546, Nov. 1982.
- [25] H. Mokhtari and P. Lazaridis, "Comparative study of lateral profile knife-edge diffraction and ray tracing technique using gtd in urban environment," *IEEE Transactions on Vehicular Technology*, vol. 48, no. 1, pp. 255–261, Jan. 1999.
- [26] C. Tzaras and S. R. Saunders, "Comparison of multiple-diffraction models for digital broadcasting coverage prediction," *IEEE Transactions on Broadcasting*, vol. 46, no. 3, pp. 221–226, Sep. 2000.
- [27] D. B. Smith, D. Miniutti, T. A. Lamahewa, and L. W. Hanlen, "Propagation models for body-area networks: A survey and new outlook," *IEEE Antennas and Propagation Magazine*, vol. 55, no. 5, pp. 97–117, 2013.
- [28] G. Koutitas, "Multiple human effects in body area networks," *IEEE Antennas and Wireless Propagation Letters*, vol. 9, pp. 938–941, 2010.
- [29] A. D. C. de Queiroz and L. C. Trintinália, "An analysis of human body shadowing models for ray-tracing radio channel characterization," in *Microwave and Optoelectronics Conference (IMOC), 2015 SBMO/IEEE MTT-S International*. IEEE, 2015, pp. 1–5.
- [30] N. Cho, J. Yoo, S.-J. Song, J. Lee, S. Jeon, and H.-J. Yoo, "The human body characteristics as a signal transmission medium for intrabody communication," *IEEE Transactions on Microwave Theory and Techniques*, vol. 55, no. 5, pp. 1080–1086, May 2007.
- [31] C. Andreu, S. Castelló-Palacios, C. Garcia-Pardo, A. Fornes-Leal, A. Vallés-Lluch, and N. Cardona, "Spatial in-body channel characterization using an accurate uwb phantom," *IEEE Transactions on Microwave Theory and Techniques*, vol. 64, no. 11, pp. 3995–4002, 2016.
- [32] Y. Nechayev, P. Hall, and Z. Hu, "Characterisation of narrowband communication channels on the human body at 2.45 ghz," *IET Microwaves Antennas Propagation*, vol. 4, no. 6, pp. 722–732, June 2010.
- [33] A. Fort, J. Ryckaert, C. Desset, P. De Doncker, P. Wambacq, and L. Van Biesen, "Ultra-wideband channel model for communication around the human body," *IEEE Journal on Selected Areas in Communications*, vol. 24, no. 4, pp. 927–933, April 2006.
- [34] L. Liu, P. De Doncker, and C. Oestges, "Fading correlation measurement and modeling on the front side of a human body," in *Antennas and Propagation, 2009. EuCAP 2009. 3rd European Conference on*. IEEE, 2009, pp. 969–973.
- [35] M. Ghaddar, L. Talbi, T. Denidni, and A. Sebak, "A conducting cylinder for modeling human body presence in indoor propagation channel," *Antennas and Propagation, IEEE Transactions on*, vol. 55, no. 11, pp. 3099–3103, Nov. 2007.
- [36] B. Hamilton, M. Xiaoli, R. Baxley, and S. Matechik, "Propagation modeling for radio frequency tomography in wireless networks," *IEEE Journal of Selected Topics in Signal Processing*, vol. 8, no. 1, pp. 55–65, Feb. 2014.
- [37] H. Yiğitler and R. Jäntti, "Experimental accuracy assessment of radio tomographic imaging methods," in *Pervasive Computing and Communication Workshops (PerCom Workshops), 2016 IEEE International Conference on*. IEEE, 2016, pp. 1–6.
- [38] A. Eleryan, M. Elsabagh, and Y. M., "Synthetic generation of radio maps for device-free passive localization," in *Proceedings of the Global Telecommunication Conference (GLOBECOM 2011)*, Dec. 2011, pp. 1–5.
- [39] B. Kibret, A. K. Teshome, and D. T. Lai, "Characterizing the human body as a monopole antenna," *IEEE Transactions on Antennas and Propagation*, vol. 63, no. 10, pp. 4384–4392, 2015.
- [40] K. I. Ziri-Castro, W. G. Scanlon, and N. E. Evans, "Prediction of variation in mimo channel capacity for the populated indoor environment using a radar cross-section-based pedestrian model," *IEEE Transactions on Wireless Communications*, vol. 4, no. 3, pp. 1186–1194, 2005.
- [41] M. Yokota, K. Shiiya, Y. Ohta, and T. Fujii, "Propagation loss properties in case human bodies exist between transmitter and receiver," in *Antennas and Propagation (ISAP), 2012 International Symposium on*. IEEE, 2012, pp. 343–346.
- [42] M. Mohamed, M. Cheffena, A. A. Moldsvor, and F. P. P. Fontan, "Physical-statistical channel model for off-body area network," *IEEE Antennas and Wireless Propagation Letters*, pp. pre-print, 2017.
- [43] V. Rampa, G. G. Gentili, S. Savazzi, and M. D'Amico, "Em models for passive body occupancy inference," *IEEE Antennas and Wireless Propagation Letters*, vol. PP, no. 99, pp. 1–4, Jul. 2017.
- [44] P. Hillyard and N. Patwari, "Never use labels: Signal strength-based bayesian device-free localization in changing environments," *IEEE Transactions on Mobile Computing*, vol. 19, no. 4, pp. 894–906, 2020.
- [45] V. Rampa, S. Savazzi, M. D'Amico, and G. G. Gentili, "Dual-target body model for device-free localization applications," in *2019 IEEE-APS Topical Conference on Antennas and Propagation in Wireless Communications (APWC)*, 2019, pp. 181–186.
- [46] S. W. Lee, "Path integrals for solving some electromagnetic edge diffraction problems," *Journal of Mathematical Physics*, vol. 19, no. 6, pp. 1414–1422, 1978.

- [47] G. Durgin, "The practical behavior of various edge-diffraction formulas," *IEEE Antennas and Propagation Magazine*, vol. 51, no. 3, pp. 24–35, June 2009.
- [48] J. Deygout, "Correction factor for multiple knife-edge diffraction," *IEEE Transactions on Antennas and Propagation*, vol. 39, no. 8, pp. 1256–1258, Aug. 1991.
- [49] V. Rampa, S. Savazzi, M. Nicoli, and M. D'Amico, "Physical modeling and performance bounds for device-free localization systems," *IEEE Signal Processing Letters*, vol. 22, no. 11, pp. 1864–1868, 2015.
- [50] R. Luebbers, "Finite conductivity uniform gtd versus knife edge diffraction in prediction of propagation path loss," *IEEE Transactions on Antennas and Propagation*, vol. 32, no. 1, pp. 70–76, Jan. 1984.
- [51] M. Ghaddar, L. Talbi, T. Denidni, and A. Charbonneau, "Modeling human body effects for indoor radio channel using utd," in *Electrical and Computer Engineering, 2004. Canadian Conference on*, vol. 3. IEEE, 2004, pp. 1357–1360.
- [52] E. Reusens, W. Joseph, G. Vermeeren, L. Martens, B. Latré, I. Moerman, B. Braem, and C. Blondia, "Path loss models for wireless communication channel along arm and torso: measurements and simulations," in *Antennas and Propagation Society International Symposium, 2007 IEEE*. IEEE, 2007, pp. 345–348.
- [53] B. Davis and G. Brown, "Diffraction by a randomly rough knife edge," *IEEE Transactions on Antennas and Propagation*, vol. 50, no. 12, pp. 1769–1778, Dec. 2002.
- [54] ITU-R, "Recommendation ITU-R P.1238-10," Propagation data and prediction methods for the planning of indoor radiocommunication systems and radio local area networks in the frequency range 900 MHz to 100 GHz, P Series Radiowave propagation, Aug. 2019.
- [55] S. Savazzi, M. Nicoli, F. Carminati, and M. Riva, "A Bayesian approach to Device-Free Localization: Modeling and experimental assessment," *IEEE Journal of Selected Topics in Signal Processing*, vol. 8, no. 1, pp. 16–29, Feb. 2014.
- [56] A. Coulson, A. Williamson, and R. Vaughan, "A statistical basis for lognormal shadowing effects in multipath fading channels," *IEEE Transactions on Communications*, vol. 46, no. 4, pp. 494–502, Apr. 1998.
- [57] A. Z. Elsherbeni, P. Nayeri, and C. Reddy, *Antenna Analysis and Design using FEKO Electromagnetic Simulation Software, The ACES Series on Computational Electromagnetics and Engineering (CEME)*. SciTech Publishing, 2014.
- [58] "IEEE Standard for Local and metropolitan area networks—Part 15.4: Low-Rate Wireless Personal Area Networks (LR-WPANs) Amendment 1: MAC sublayer," *IEEE Std 802.15.4e-2012 (Amendment to IEEE Std 802.15.4-2011)*, pp. 1–225, April 2012.
- [59] S. Savazzi, V. Rampa, F. Vicentini, and M. Giussani, "Device-free human sensing and localization in collaborative human–robot workspaces: A case study," *IEEE Sensors Journal*, vol. 16, no. 5, pp. 1253–1264, 2016.
- [60] NXP Laboratories (UK), "Data-sheet JN-DS-JN5148-001: IEEE 802.15.4 Wireless Microcontroller JN5148-001," https://www.nxp.com/docs/en/brochure/JN5148_PB_1v4.pdf, 2010.
- [61] Y. Chen and A. Terzis, "On the mechanisms and effects of calibrating rssi measurements for 802.15.4 radios," in *European Conference on Wireless Sensor Networks (EWSN)*, 2010, pp. 256–271.
- [62] V. Rampa, S. Savazzi, and S. Kianoush, "Physical model-based calibration for device-free radio localization and motion tracking," in *2019 IEEE-APS Topical Conference on Antennas and Propagation in Wireless Communications (APWC)*, 2019, pp. 353–358.